

Sulfate Respiration in *Desulfovibrio vulgaris* Hildenborough

STRUCTURE OF THE 16-HEME CYTOCHROME *c* HmcA AT 2.5-Å RESOLUTION AND A VIEW OF ITS ROLE IN TRANSMEMBRANE ELECTRON TRANSFER*

Received for publication, July 25, 2002

Published, JBC Papers in Press, September 27, 2002, DOI 10.1074/jbc.M207465200

Pedro M. Matias‡, Ana V. Coelho‡§, Filipa M. A. Valente‡, Diana Plácido‡, Jean LeGall‡¶, António V. Xavier‡, Inês A. C. Pereira‡, and Maria Arménia Carrondo‡||

From the ‡Instituto de Tecnologia Química e Biológica, Universidade Nova de Lisboa, Av. da República, EAN, Apartado 127, Oeiras 2781-901, Portugal, the §Chemistry Department, Universidade de Évora, Apartado 94, 7001 Évora Codex, Portugal, and the ¶Department of Biochemistry and Molecular Biology, University of Georgia, Athens, Georgia 30602

The crystal structure of the high molecular mass cytochrome *c* HmcA from *Desulfovibrio vulgaris* Hildenborough is described. HmcA contains the unprecedented number of sixteen hemes *c* attached to a single polypeptide chain, is associated with a membrane-bound redox complex, and is involved in electron transfer from the periplasmic oxidation of hydrogen to the cytoplasmic reduction of sulfate. The structure of HmcA is organized into four tetraheme cytochrome *c*₃-like domains, of which the first is incomplete and contains only three hemes, and the final two show great similarity to the nine-heme cytochrome *c* from *Desulfovibrio desulfuricans*. An isoleucine residue fills the vacant coordination space above the iron atom in the five-coordinated high-spin Heme 15. The characteristics of each of the tetraheme domains of HmcA, as well as its surface charge distribution, indicate this cytochrome has several similarities with the nine-heme cytochrome *c* and the Type II cytochrome *c*₃ molecules, in agreement with their similar genetic organization and mode of reactivity and further support an analogous physiological function for the three cytochromes. Based on the present structure, the possible electron transfer sites between HmcA and its redox partners (namely Type I cytochrome *c*₃ and other proteins of the Hmc complex), as well as its physiological role, are discussed.

the respiration of sulfate. The product of this respiration, sulfide, is highly toxic and corrosive and is responsible for the environmental, economic, and health impact of these bacteria in their habitats: soil, still and freshwaters, seawater, the human (and other animal) colon, and oil fields and pipelines (1, 2). The sulfate respiratory chain is still one of the least understood anaerobic respiration processes. One of its peculiarities is that the terminal reductases responsible for reduction of sulfate are all cytoplasmic and thus do not contribute directly to creation of a proton gradient across the membrane. Hydrogen seems to be an important component in the metabolism of SRB. It can be used as the sole energy source by several bacteria (3), and it is formed during growth in the absence of sulfate (4). Hydrogen is also transiently produced and then consumed during growth on organic compounds in the presence of sulfate (5, 6). It has been proposed that energy conservation in SRB involves H₂ as an intermediate, which is formed in the cytoplasm as a result of oxidative metabolism, and diffuses to the periplasm where its reoxidation generates electrons that are shuttled across the membrane for the reduction of sulfate, leaving protons in the periplasm to activate the ATP synthase (7, 8).

Desulfovibrio is the best studied genus of SRB. The bacteria of this genus are characterized by having an unusual number of periplasmic multiheme cytochromes, of which the most abundant and widespread is the well characterized tetraheme Type I cytochrome *c*₃ (TpI-*c*₃) (9), which is thought to play a central role in the respiratory chain and act as a physiological partner for hydrogenases. Other examples include the sixteen-heme high molecular mass cytochrome *c* (HmcA) (10–14), the nine-heme cytochrome *c* (9HcA) (15–17), the tetraheme type II cytochrome *c*₃ (TpII-*c*₃), which differs from the TpI-*c*₃ in structural, functional, and genetic terms (18), the octaheme cytochrome *c*₃ (*M*_r 26,000), a dimer of a tetraheme subunit (19), and the dimeric split-Soret cytochrome *c*, which is a dimer of a diheme subunit (20). HmcA has sixteen hemes *c* and a mass of ~65 kDa. It was isolated as a soluble protein from *Desulfovibrio vulgaris* Hildenborough (DvH) (10, 11), *D. vulgaris* Miyazaki (DvM) (12), and *Desulfovibrio gigas* (Dg) (13), but it can be found in higher amounts in the membrane fraction (14). The gene for HmcA was cloned in DvH, and it was found to be part of a large operon (the *hmc* operon) encoding a putative membrane-bound redox complex of six proteins, HmcA–HmcF (21). HmcA is a hydrophilic cytochrome with no transmembrane helices and contains a signal peptide indicating that it is periplasmic; HmcB is a putative 40.1-kDa transmembrane protein having a periplasmic hydrophilic N-terminal domain with four Fe₄S₄ cluster binding motifs and a cytoplasmic C-terminal tail (22); HmcC (43.2 kDa), HmcD (5.8 kDa), and HmcE (25.3

Sulfate reducing bacteria (SRB)¹ are a broad group of bacteria that have in common the fact that they derive energy from

* This work was supported by Fundação para a Ciência e Tecnologia grants POCTI/36562/ESP/2000 (to I. A. C. P.), POCTI/35021/BME/1999 (to A. V. X.), and PRAXIS/P/BIO/12080/1998 (to P. M. M. and M. A. C.). The costs of publication of this article were defrayed in part by the payment of page charges. This article must therefore be hereby marked "advertisement" in accordance with 18 U.S.C. Section 1734 solely to indicate this fact.

The atomic coordinates and structure factors (code 1h29 and r1h29sf) have been deposited in the Protein Data Bank, Research Collaboratory for Structural Bioinformatics, Rutgers University, New Brunswick, NJ (<http://www.rcsb.org/>).

|| To whom correspondence should be addressed. Tel.: 351-21-446-9657; Fax: 351-21-443-3644; E-mail: carrondo@itqb.unl.pt.

¹ The abbreviations used are: SRB, sulfate reducing bacteria; DvH, *D. vulgaris* Hildenborough; Dg, *D. gigas*; Dd27k, *D. desulfuricans* ATCC27774; DdE, *D. desulfuricans* Essex 6; Da, *D. africanus*; Dac, *D. acetoxidans*; HmcA, 16-heme high molecular mass cytochrome; cyt.*c*₃, tetraheme cytochrome *c*₃; Tpl-*c*₃, Type I tetraheme cytochrome *c*₃; TplII-*c*₃, Type II tetraheme cytochrome *c*₃; cyt.*c*₇, triheme cytochrome *c*₃ from Dac; 9HcA, 9-heme cytochrome *c*; PDB, Protein Data Bank; ITQB, Instituto de Tecnologia Química e Biológica; NCS, non-crystallographic symmetry; ESRF, European Synchrotron Radiation Facility; MAD, multiwavelength anomalous dispersion.

kDa) are all predicted to be integral membrane proteins, of which HmcC and HmcE may bind hemes *b*, and HmcF is predicted to be a 52.7-kDa membrane-associated cytoplasmic protein having two Fe₄S₄ cluster binding motifs. The Hmc complex has been proposed to constitute the missing link between periplasmic hydrogen oxidation and cytoplasmic sulfate reduction (21), accepting electrons from the hydrogenases via the TpI-c₃ and transferring them across the membrane to the cytoplasm for reduction of sulfate. This role of the Hmc complex is corroborated by growth and expression studies with wild type and mutant strains of SRB (23–25) and by electron transfer experiments (26).

HmcA is the cytochrome with the highest number of hemes in a single polypeptide, known so far. It is the largest in the family of periplasmic *Desulfovibrio* cytochromes and was the only one, until now, for which no structure was available. In this report we describe the crystal structure of the DvH HmcA and analyze the implications of this structure in terms of the physiological role of this cytochrome in the sulfate respiratory pathway.

EXPERIMENTAL PROCEDURES

Protein Purification and Crystallization—Cells were grown, and the 16-heme HmcA cytochrome was purified following the protocol previously described (14). The purity of the protein solution was checked by SDS-PAGE. Crystallization conditions were screened using the hanging drop vapor diffusion method, but larger crystals could only be obtained using the dialysis method. The composition of the crystallization solution was: 40% 2-propanol (v/v), 0.1 M Tris-HCl buffer, pH 7.5. The addition of several additives (*e.g.* 2-methyl-2,4-pentanediol (MPD), ethanol, dioxane, and detergents) to this crystallization solution did not seem to improve the crystal quality. Each crystallization assay was prepared by adding 5 μl of the protein solution (10 mg·ml⁻¹) to a dialysis button, which was then completely soaked in the crystallization solution. After a few days at 4 °C small hexagonal bipyramids started to appear and reached their maximum size after 1 week. The best cryocrystallography conditions were obtained by soaking these crystals in a crystallization solution containing 7.5% MPD.

Data Collection and Structure Determination—The diffraction pattern from HmcA crystals indicated that they belong to one of the hexagonal space groups P6₂ or P6₄, with cell constants *a* = 220.39, *c* = 102.64 Å at 100 K. The presence of four molecules in the asymmetric unit was suggested by *V_m* considerations (27), resulting in a solvent content of about 60%. Crystals of HmcA were pre-frozen at ITQB and shipped frozen to the ESRF in Grenoble, France, where a three-wavelength MAD experiment was carried out at beamline ID-29. Two of the energies (peak and inflection point) were chosen by inspection of an x-ray fluorescence spectrum from a crystal, taken near the K-absorption edge of iron. A third energy (remote) was chosen as 13.51 KeV. The experiment was designed to obtain a three-wavelength MAD data set about 80% complete (in terms of Bijvoet pairs) to 3.0 Å. This non-optimal strategy was caused by the observation that, because even the best crystals showed clear evidence of crystal multiplicity, only a relatively small oscillation range could provide usable diffraction data. Notwithstanding, and in view of the relatively high iron content of this protein, it was thought that this data set would be sufficient to solve the HmcA structure. Additionally, a very fine beam size (30 × 30 μm) combined with a fine ϕ -slicing (0.25°) were used to minimize spatial overlap between the diffraction spots, and, to minimize the chances of radiation damage as well as the number of saturated reflections on the diffracted images, the incident beam intensity was greatly reduced by reducing the primary horizontal guard to 0.25 mm. The ADSC-Q4R detector on ID-29 was used to record the diffraction images, which were processed using the HKL suite (DENZO/SCALEPACK) (28). The statistics of x-ray data collection and processing are summarized in Table I.

Although the values for *R_{anom}* were not significantly higher than *R_{merge}* for the data collected at the peak point of inflection wavelengths, the presence of anomalous signal at these wavelengths was made clear by the “compareano” protocol in SCALEPACK. Respectively, overall χ^2 values of 5.5 and 2.7 were observed, when comparing the mean diffraction intensities of the two members of each complete Bijvoet pair, following χ^2 value adjustment to near unity in successive scaling, merging, and outlier rejecting rounds where they were treated as separate

TABLE I
Summary of data collection, processing, scaling, and phasing statistics

Values in parentheses refer to the last resolution shell, 2.90 ≥ *d* ≥ 2.80 Å for λ_1 and λ_2 , 2.59 ≥ *d* ≥ 2.50 Å for λ_3 . $R_{\text{merge}} = \sum_i \sum_j |I_i - \langle I \rangle| / \sum_i I_i$; $R_{\text{anom}} = \sum_h |I^+ - I^-| / \sum_h [(I^+ + I^-) / 2]$. The multiplicity values are overall values, *i.e.* no distinction is made between Bijvoet pairs. The percent Bijvoet completeness figure is calculated as the ratio between the number of pairs recorded and the total number of acentric reflexions measured. Scaling $R_{\text{factor}} (F) = \sum_{\text{hkl}} |F_{\lambda_i} - F_{\lambda_j}| / \sum_{\text{hkl}} F_{\lambda_j}$.

Wavelength	λ_1 , 1.7418 Å (peak)	λ_2 , 1.7445 Å, (point of inflection)	λ_3 , 0.9179 Å (remote)
Resolution limits (Å)	25.0–2.80	25.0–2.80	25.0–2.50
<i>N</i> _{reflections}	62,478	62,314	89,606
% completeness	87.3 (75.6)	87.6 (76.9)	91.3 (84.0)
% Bijvoet completeness	84.2 (82.7)	85.3 (84.5)	87.8 (88.4)
Multiplicity	6.2	6.3	6.5
<i>R_{merge}</i>	0.089 (0.341)	0.076 (0.316)	0.064 (0.354)
<i>R_{anom}</i>	0.088 (0.278)	0.055 (0.208)	0.034 (0.177)
Anomalous χ^2	5.5	2.7	1.3
Overall <i>I</i> / σ (<i>I</i>)	9.8	11.2	11.9
Wilson plot <i>B</i> (Å ²)	71.9	73.7	58.1
Scaling <i>R_{factor}</i> (<i>F</i>)	0.078	0.093	
Phasing power, acentric	0.92		2.06
Phasing power, centric	0.47		1.35
Acentric <i>R_{cullis}</i>	0.83		0.59
Centric <i>R_{cullis}</i>	0.90		0.53
Anomalous <i>R_{cullis}</i>	0.71	0.78	0.92

reflections. The scaled and merged data for the three wavelengths were then converted to CCP4 format (29) for further processing and analysis. The program SCALEIT was used to scale together the three data sets, using the remote as reference. Patterson maps were calculated using as coefficients the anomalous differences for the peak and point of inflection wavelengths, as well as the dispersive differences between the remote and point of inflection wavelengths. In these maps, many strong peaks could be seen in the *w* = 0 section, the largest feature being located at about (0, 1/2) (1/2, 0) and (1/2, 1/2) in the (*u,v*) plane. This was interpreted as being the result of a 2-fold non-crystallographic symmetry (NCS) axis parallel to the 6-fold crystallographic axis. 64 iron atoms from the 16 heme groups in each of the 4 independent molecules were expected in the asymmetric unit, and this large number of anomalous scatterers recommended a direct method approach using the Shake & Bake protocol (30) to determine their positions. Using the peak wavelength data and 1000 sets of randomly generated atoms in space group P6₂, the resulting *R_{min}* histogram clearly showed a bi-modal distribution, an indication of a correct (albeit partial) determination of the iron sub-structure in the HmcA crystal structure. The same procedure was carried out in space group P6₄ and failed to produce a similar distribution of the *R_{min}* histogram. This was interpreted as the resolution of the space group ambiguity in favor of P6₂. To minimize the chances of introducing spurious peaks in the MAD phasing procedure, only the top 32 sites were used to begin phase refinement calculations with MLPHARE (31). Dispersive difference Fourier maps, calculated using MLPHARE phases and difference amplitudes between the remote and point of inflection data sets as coefficients, were used to locate additional iron sites, which were then added to the phase calculation and refinement procedure. These maps were found to be in this case more useful than Fourier maps calculated with MLPHARE phases (retarded by 90°) and the peak wavelength anomalous differences as coefficients, because more peaks were observed and a clearer distinction between true and spurious peaks could be achieved. In this way, all 64 iron sites in the asymmetric unit were located and included in the MLPHARE phase refinement procedure, which at convergence gave phases to 2.8 Å with an overall figure of merit of 0.589. These phases were further improved to $\langle m \rangle = 0.699$ up to 2.5-Å resolution with DM (32) using phase extension, histogram matching, solvent flattening, and NCS averaging protocols. Using these 64 sites, a phasing and density modification procedure using SOLVE (33) and RESOLVE (34) was also carried out resulting in a final overall figure of merit of 0.684 up to 2.5-Å resolution. Electron density maps calculated at 2.5-Å resolution using phases from both procedures were used to build an initial model for the HmcA molecule with programs O (35) and TURBO-PRODO (36). The main statistics of the phasing process are listed in Table I.

Refinement of the 16-Heme HmcA Structure—A nearly perfect 4-fold NCS was assumed for the asymmetric unit of the HmcA crystal structure; therefore, the initial model of the HmcA molecule was built for

TABLE II
Final refinement statistics for HmcA

Resolution limits (Å)	25.0–25.1			
R-factor (%) [85,075 reflections, no $\sigma(F_o)$ cutoff]	19.2			
Free R-factor (%) [4,494 reflections, no $\sigma(F_o)$ cutoff]	25.8			
Number of non-hydrogen protein atoms	17,794			
Number of solvent molecules	497			
Maximum likelihood estimate of overall coordinate error (Å)	0.23			
Model r.m.s. deviations from ideality	Bond lengths (Å)	Bond angles (°)	Planar groups (Å)	Chiral centers (Å ³)
	0.014	1.55	0.005	0.099
	Molecule A	Molecule B	Molecule C	Molecule D
Model completeness				
Zero occupancy non-hydrogen atoms	38	75	90	70
Whole residues omitted from model	32–37	32–37	32–37	32–37
	500–504	500–504	500–505	283–285
	544–545	542–545	545	394–397
				500–505
				543–545
Average B values (Å ²) ^a				
Main-chain protein	67.5	63.2	61.1	67.6
Side-chain protein	68.8	64.3	62.2	68.6
Heme groups	56.9	53.4	52.7	58.0
Solvent molecules			59.7	

^a Calculated from equivalent isotropic B values, including the TLS contribution for the protein atoms.

only one of the four independent molecules and the coordinates for the other three molecules were then obtained from those of the first by applying the appropriate NCS operations, derived from the positions of the 16 iron atoms in each molecule. We adopted a residue-numbering scheme based on the full protein sequence (including the signal peptide) (21), and therefore the mature protein begins at residue 32. The structure was refined using X-PLOR (37). In all refinement stages and map calculations, a bulk solvent correction was used, and all low resolution data were included. Prior to the refinement calculations, a random 5% sample of the reflection data was flagged for R_{free} calculations (38). All model interactive visualization and editing was carried out using TURBO-Frodo (36). Data up to 2.5 Å and 4-fold NCS restraints were used in the initial refinement. This refinement converged to R and R_{free} values of 22.7% and 30.3%, respectively. The use of 2-fold NCS restraints did not improve these values significantly; therefore, at this point, a 2.5-Å refinement without any imposed NCS restraints was carried out. In addition to the $2|F_o| - |F_c|$ and $|F_o| - |F_c|$ electron density maps calculated with X-PLOR, $2|F_o| - |F_c|$ electron density maps were obtained by applying the fast ARP/wARP (39, 40) molecular replacement protocol to the X-PLOR refinement results, and $|F_o| \sigma_A$ maps (41) were computed by phase recombination of the original SOLVE phases with the model phases from X-PLOR (downweighted by 0.816). Careful inspection of these maps revealed a breakdown of the assumed NCS, in particular for two clearly defined regions in each molecule: residues 282–290, and neighboring 389–397, due to different crystal packing environments. The four molecules were rebuilt taking these differences into account, and further refinement with X-PLOR, without any imposed NCS restraints, resulted in a marked decrease in R_{free} (from 30.3% to 28.7%). The final refinements were carried out with REFMAC (42) using TLS (43) rigid body refinement prior to restrained refinement of atomic positions and thermal motion parameters. For each independent molecule in the asymmetric unit, three rigid bodies were defined, corresponding to the three major structural domains (see “Discussion”): triheme cytochrome c_3 , tetraheme cytochrome c_3 , and nine-heme cytochrome c . In the final refinement, 497 water molecules were included in the model, and individual restrained B-factors were refined for all non-hydrogen atoms. The final values of R and R_{free} were 19.2% and 25.8%, respectively. In each of the four independent HmcA molecules there were some regions where the electron density was either unclear or missing, and therefore some atoms were given zero occupancy in the refinement. In some cases, whole residues had to be left out of the model. The final refinement results and statistics are shown in Table II.

Data Deposition—Coordinates and structure factors have been deposited with the Protein Data Bank (44) with Protein Data Bank accession codes 1h29 and r1h29sf, respectively.

RESULTS AND DISCUSSION

Structure Analysis—The 16-heme HmcA crystallizes as a dimer, there being two such dimers in the asymmetric unit. The molecules in each dimer are related (with the exceptions

noted above) by a 2-fold NCS axis parallel to the crystallographic 6_2 screw axis. There are also 2-fold NCS axes as well as pure translations relating the two independent dimers. The combination of these crystallographic and NCS elements results in very strong peaks being observed in both native, anomalous and dispersive Patterson maps and also in strong 2-fold NCS axes perpendicular to the crystallographic 6_2 screw axis, observed in self-rotation Patterson maps. The dimerization results from two specific intermolecular interactions: Asp-132 O^{δ2} and Glu-134 O^{ε2} in the first monomer, respectively, form a hydrogen bond (2.9 Å) with His-516 N^{δ1} and an electrostatic interaction (3.0 Å) with Asn-533 N^{δ2} in the second monomer, and vice versa. His-516 is one of the heme 16 axial ligands, whereas Asn-533 N^{δ2} already has an intramolecular hydrogen bond to Asp-524 O^{δ1}. Only 3% of the total molecular surface of each monomer, *i.e.* 850 Å² in 27780 Å², calculated with AREAIMOL (29) are buried by the dimerization process. The R_{free}/R ratio of 1.34 is within the expected range for the number of atoms, refined parameters, and reflections used in the 2.5-Å resolution refinement (45). The TLS refinement with REFMAC lowered both R and R_{free} (0.192 and 0.258), in comparison with X-PLOR (0.203, 0.290) and REFMAC (0.205, 0.279) refinements without TLS. Curiously, the TLS refinement gave rise to higher B-values for the protein than had been obtained with the X-PLOR and REFMAC refinements without TLS. The anisotropic thermal motion parameters derived from the REFMAC TLS refinement with TLSANL (29) are represented in Fig. 1, and it can be seen that, within the limitations of the data resolution and of the TLS rigid group definition used, the protein regions with highest and most anisotropic B-values are located, as expected, in loop regions exposed to the solvent. Interestingly, the polypeptide segment connecting the top and bottom of the nine-heme region of HmcA also exhibits high thermal motion parameters, an indication of its flexibility. The four independent HmcA molecules in the crystal structure were analyzed with PROCHECK (46), and their stereochemical quality parameters were within their respective confidence intervals. In the Ramachandran (47) ϕ, ψ plot, between 83.5% and 85.7% of the residues lie within the most favored regions, and there are only three residues (Asp-212 and Ala-395 in molecule A, Ala-390 in molecule B) that are marginally inside the disallowed regions. A few (between 1 and 5) close contacts (2.5–2.6 Å) were reported by PROCHECK. All molecules were

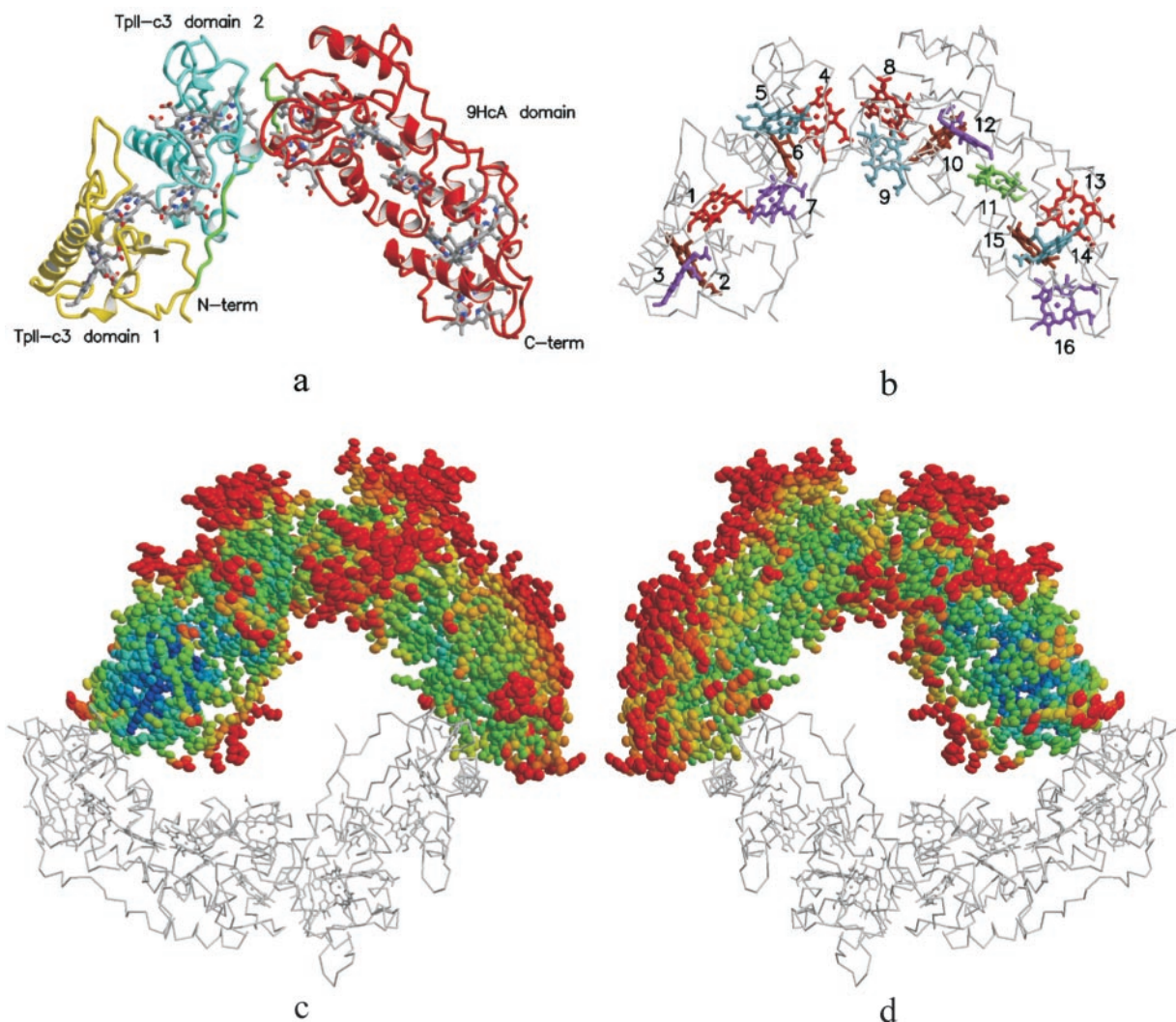


FIG. 1. Diagrams of the three-dimensional structure of the 16-heme HmcA showing (a) the protein chain fold and the domains, (b) the heme numbering scheme, (c and d) the anisotropic thermal motion parameters derived for monomer A from the REFMAC TLS refinement. The heme colors in b reflect their correspondence with the hemes in cyt.c₃ as discussed in the text: heme 1 (red), heme 2 (light blue), heme 3 (brown), and heme 4 (purple). The isolated heme group in the 9HcA domain of HmcA is drawn in green. The molecule orientation in c is the same as in a, and in d it is rotated by 180° about a vertical axis in the plane of the figure. The atomic thermal motion ellipsoids are drawn at the 25% probability level. Dark blue atoms have B_{eq} (equivalent isotropic B) below 40.0 Å², light red atoms have B_{eq} above 80.0 Å², and atoms with intermediate values of B_{eq} were assigned colors with hues varying smoothly through the spectrum from blue to red. The second monomer in the represented dimer is drawn as a $C\alpha$ -trace for the polypeptide chain, and its heme groups are represented using sticks. These graphics were prepared with Molscript, Rastep, and Raster3D (61, 62).

assigned to class (1 2 2) (48), and their overall G -factors ranged between -0.02 and -0.07 .

Domain Structure of the 16-Heme HmcA—The tetraheme cytochromes TpI-c₃ and TpII-c₃ have a four-heme structural motif that is also observed in other periplasmic *Desulfovibrio* cytochromes (with the exception of the Split-Soret cytochrome), and it has been proposed, on the basis of sequence alignments, that DvH HmcA is formed by four cyt.c₃-like domains, the first one being an incomplete domain with only three hemes and with heme 12 being a high-spin heme (11). The structure of the *Desulfovibrio desulfuricans* ATCC 27774 (Dd27k) 9HcA cytochrome revealed that this cytochrome is also composed of two tetraheme motifs with an isolated heme (heme 4 of 9HcA) between them (16). Furthermore, sequence alignment between the 9HcA and the last two domains of DvH HmcA indicated a high similarity between them and led to the proposal that heme 11 of Hmc would be an isolated heme between the last two domains and that heme 15 would be the high-spin heme (16). All these predictions have been confirmed in the present structure. As shown in Fig. 1, the HmcA structure can be divided

into four cyt.c₃-like domains, with the first one containing only three hemes (residues 38–143), the second containing the usual four-heme motif (residues 153–258) and with the last two forming a nine-heme 9HcA-like domain (residues 268–545), which includes the isolated heme group. For simplicity, we have chosen to regard this last region as a single domain, which has been already fully characterized (15–17) rather than further sub-dividing it into two cyt.c₃ domains. These domains are spatially arranged in such a way that the molecule can be described as made up of two different regions: an N-terminal region that comprises the first two domains and a C-terminal region that comprises the 9HcA domain. The N-terminal region has an approximate length of 59 Å, whereas the C-terminal region extends for nearly 70 Å. The angle between these regions is about 77°, thus giving the 16-heme HmcA molecule the shape of a stretched “V,” where one leg is the N-terminal region, the other leg the C-terminal region, and the distance between the ends of the legs is ~87 Å. This spatial arrangement and the way the protein chain in each domain is tightly bound around its heme core, with the domains being connected

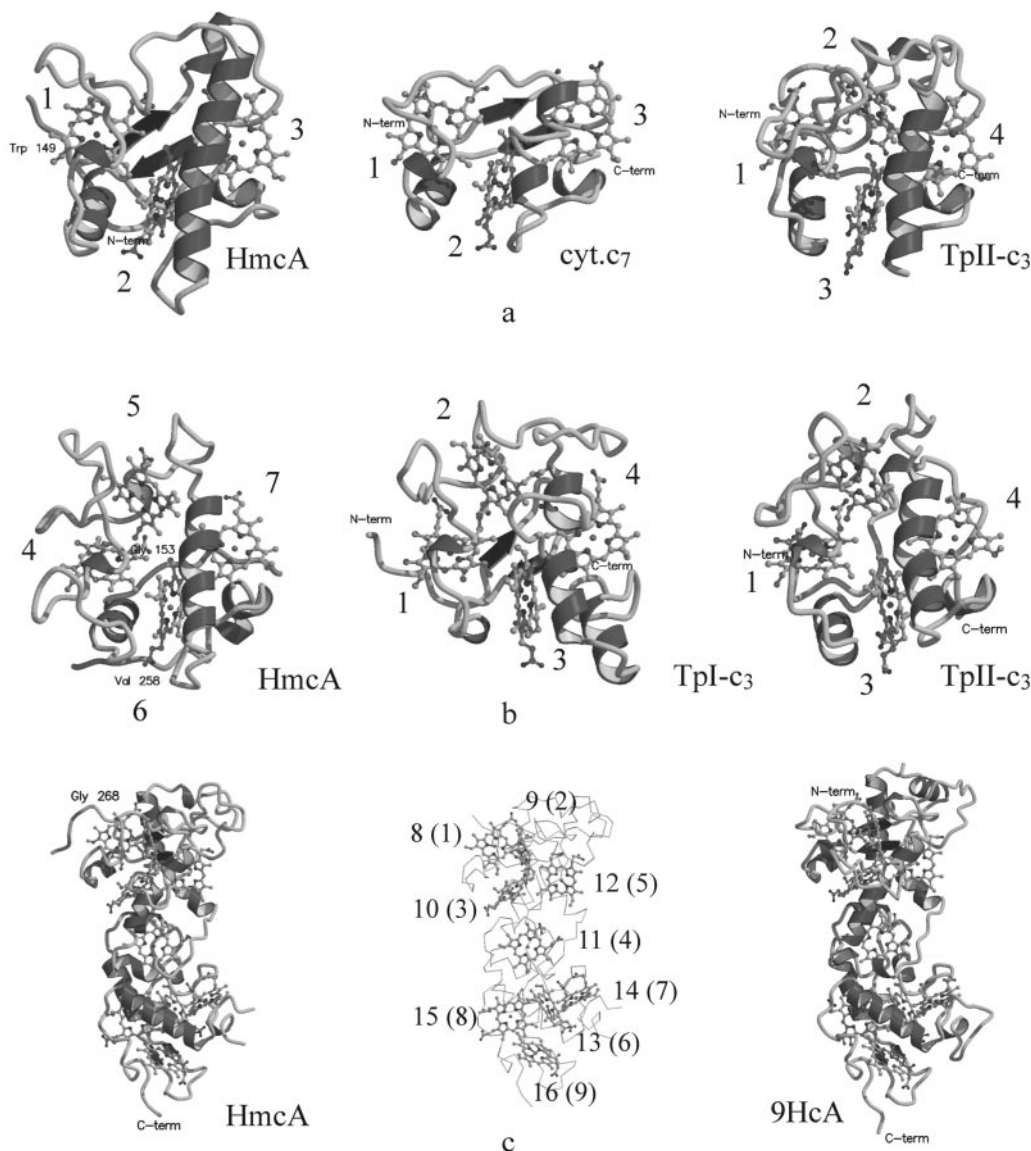


FIG. 2. Side-by-side comparison between the different domains in the three-dimensional structure of the 16-heme HmcA and the three-dimensional structures of *cyt.c₇*, *cyt.c₃*, and 9HcA. *a*, triheme domain versus *cyt.c₇* and TpII-*c₃*; *b*, tetraheme domain versus Tpl-*c₃* and TpII-*c₃*; *c*, nine-heme domain versus 9HcA. For clarity, heme numbers in *c* are given in a separate picture, with 9HcA heme numbers given in parentheses following the corresponding HmcA heme number. The graphics were prepared with Molscript and Raster3D (61, 62).

by extended segments of polypeptide chain, also suggest a high degree of flexibility for this molecule.

An interesting aspect of HmcA is that the heme groups of the first two domains are arranged contrary to what would be expected from the protein sequence (see Fig. 1). Indeed, the N terminus and heme 1 are not present at one extremity of the molecule, but in the region between the first two domains, and heme 4 is placed between the second and third domain, whereas it is heme 7 that is closest to the first domain. This situation is not found in the C-terminal 9HcA region in which the hemes are found according to their order in the sequence (except hemes 11 and 12; see below) with heme 16 located at the C terminus extremity. This peculiar heme arrangement of the HmcA N-terminal region results in a kind of symmetry between the heme group arrangement of the two HmcA regions, with hemes equivalent to *cyt.c₃* heme 4 (HmcA hemes 3 and 16) at each extremity of the molecule and with hemes equivalent to *cyt.c₃* heme 1 (HmcA hemes 4 and 8) at the top of the junction between the regions of the molecule.

Each of the HmcA tetraheme domains can be compared with

either of the two types of cytochromes *c₃*. The distinction between these cytochromes *c₃* is based on structural, functional, and genetic features (18). In structural terms, TpII-*c₃* can be distinguished by several local differences relative to the overall fold of Tpl-*c₃*, with the most relevant points being an exposed heme 1 surrounded by a negative surface charge, and the heme 4 lacking the characteristic surface lysine patch proposed to be the site of interaction and electron exchange of Tpl-*c₃* with a negatively charged region of hydrogenase (18, 49). This suggests that TpII-*c₃* interacts with its physiological partner via heme 1 rather than heme 4, and that its role is not to receive electrons directly from hydrogenase as is the case for Tpl-*c₃*. Indeed, kinetic experiments suggest that the electron donor to TpII-*c₃* is Tpl-*c₃* (18, 50, 51). Another interesting difference between the two types of cytochromes *c₃* is that in TpII-*c₃* all the heme-binding sites are typical in that they have two residues between the Cys that ligate the heme (CXXCH), a feature that is also observed in HmcA and 9HcA, whereas in Tpl-*c₃* the heme-binding sites for heme 2 and 4 are unusual in that they have four residues between the Cys (CX₄CH). In genetic terms,

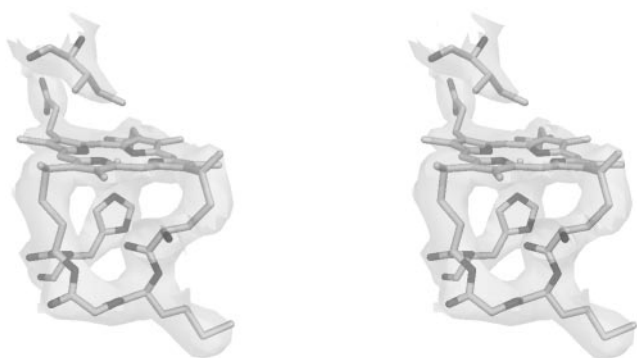


FIG. 3. Stereo view of the high-spin heme 15 in the 16-heme HmcA molecule, showing the heme binding motif Cys⁵¹⁹-Met⁵²⁰-Gly⁵²¹-Cys⁵²²-His⁵²³-Ile⁴⁵². The final $2|F_o| - |F_c|$ electron density map covering these residues and heme group is shown, drawn at the 0.8 map r.m.s. contour level. The graphics were prepared with DINO (A. Philippson (2002), available at www.dino3d.org).

the TpII-*c*₃ is encoded by a gene that is part of an operon encoding a membrane-bound redox complex (18), as found for HmcA and 9HcA, whereas all the genes for TpI-*c*₃ described so far are monocistronic. Using coordinates retrieved from the Protein Data Bank (44), a more detailed comparison is included below between the different domains of HmcA, and the TpI-*c*₃ and TpII-*c*₃ folds, as well as the integral 9HcA fold, represented by the 9HcA from Dd27k (PDB 19HC) (16). The TpI-*c*₃ structure chosen as a model for comparisons was that of DvH (PDB 2CTH) (52), and the TpII-*c*₃ structure is that of Da (PDB 3CAO) (49). A comparison of the three-heme domain with the triheme cytochrome *c*₃ (cyt.*c*₇) from *Dac* (PDB 1HH5) (53) is also included. Fig. 2 illustrates these comparisons between each of the three domains of the HmcA molecule and selected representative cytochrome molecules that contain only that domain. Overall, a higher similarity of the HmcA cyt.*c*₃ regions to the TpII-*c*₃ relative to the TpI-*c*₃, is noted, which agrees with their similarities in genetic arrangement and proposed physiological function (see below).

The Tri-heme Domain versus the Tri-heme and Tetra-heme Cytochrome *c*₃—The N-terminal triheme domain of HmcA is missing the heme corresponding to heme 2 in cyt.*c*₃, a situation that is also found in cyt.*c*₇ (54). However, this HmcA domain is more similar to cyt.*c*₃ (e.g. one of the loops that binds the second heme in cyt.*c*₃ is also present in the HmcA first domain, albeit smaller in length) than to cyt.*c*₇, which is considerably smaller (see Fig. 2a). This fact is not surprising, because, with the exception of the one from *Desulfomicrobium norvegicum*, all the known cyt.*c*₃ structures are from *Desulfovibrio* sp., whereas cyt.*c*₇ is found in different genera. The triheme domain and cyt.*c*₇ display most of the structural features that are also found in cyt.*c*₃ (see Fig. 2a): an initial loop that contains a short two-stranded anti-parallel β -sheet, a short α -helix containing the motif HXXH, the two histidine residues being the second axial ligands of hemes 1 and 2 (hemes 1 and 3 in cyt.*c*₃) and a long α -helix that contains the heme-binding motif of heme 2 (heme 3 in cyt.*c*₃) as well as the second axial histidine ligand of heme 3 (heme 4 in cyt.*c*₃). In addition, all of the heme binding motifs occur as very short (one turn or less) α -helices. In HmcA, the short α -helix is about the same size as in cyt.*c*₇ and TpII-*c*₃, whereas the long α -helix is longest in HmcA. In cyt.*c*₇, this helix is further broken into two shorter helical segments by a one-residue insertion (Ala-48). Overall, the three-heme domain in HmcA is larger than the cyt.*c*₇ molecule, not only because of the longer helices as mentioned above, but also due to the longer segments of protein chain between the first and the second β -strands (where a further short α -helix can be seen) and

between the first and second heme groups. When the two structures are superposed (not shown) it can also be seen that only hemes 2 and 3 of HmcA (corresponding to hemes 3 and 4 of cyt.*c*₃) nearly overlap with hemes 2 and 3 in cyt.*c*₇, whereas the mean plane of heme 1 in HmcA is tilted by about 30° with respect to its orientation in cyt.*c*₇; in addition, there is a 2.7-Å difference between the iron atom positions of heme 1 in the superposed structures. This marked structural difference in the vicinity of heme 1 may be caused by the smaller size of the cyt.*c*₇. In contrast, the structure of the HmcA triheme is roughly the same size as that of the TpII-*c*₃, and the superposition between these two structures (not shown) reveals a nearly perfect overlap between the three common heme groups.

The Tetra-heme Domain versus the Tetra-heme Cytochrome *c*₃—The tetraheme domain of HmcA and the structures of TpI-*c*₃ and TpII-*c*₃ contain the sequence motif CXXCHH, which comprises the heme binding region of cyt.*c*₃ heme 1 and the second axial histidine that completes the coordination of the iron atom in cyt.*c*₃ heme 2. The size of the tetraheme domain is roughly the same as that of the TpI-*c*₃ and TpII-*c*₃ molecules (see Fig. 2b). The short initial two-stranded anti-parallel β -sheet is missing from the tetraheme domain in HmcA, and it is also not observed in the structure of the TpII-*c*₃. The short α -helix has similar length in HmcA and in the TpII-*c*₃, but it is much shorter in the TpI-*c*₃. The long α -helix has similar lengths in the three structures. However, in the TpI-*c*₃ it is broken into two shorter segments connected by a loop insertion. Also, in the TpI-*c*₃ the heme 2 binding motif is of the form CX₄CH, and its structure becomes a β -turn rather than a very short α -helix.

The Nine-heme Domain versus the Nine-heme Cytochrome *c*—As previously predicted (16), the structure of the C-terminal region of HmcA is very similar to that of 9HcA. This region comprises two tetraheme clusters with a cyt.*c*₃-like fold, but with an inserted extra heme group between them. Each of the cyt.*c*₃-like regions shows the same structural characteristics mentioned above (short anti-parallel β -sheet, short α -helix, and long α -helix, see Fig. 2c). The main difference is located in the region above hemes 8, 9, and 12 (corresponding to hemes 1, 2, and 4 in cyt.*c*₃ and 1, 2, and 5 in 9HcA) where an α -helix has been partially disrupted, possibly due to interaction with a neighboring molecule in the crystal structure. This region is located near the beginning of the polypeptide segment that connects the two cyt.*c*₃-like regions in the nine-heme domain of HmcA and in the 9HcA structure. Also, there was no observed electron density for a loop region in HmcA between residues 500 and 504, suggesting a high degree of flexibility for this loop. It is interesting to note that the long α -helix in the first *c*₃-like region is broken up into two segments by an insertion of 5 residues in HmcA and 13 residues in 9HcA. This would lend some Type I similarity to this cyt.*c*₃-like region in this domain of HmcA, in contrast with all the other cyt.*c*₃-like regions in HmcA, which are clearly of Type II.

The most important difference between this HmcA domain and the 9HcA is that heme 15 (corresponding to heme 3 of cyt.*c*₃) is only coordinated by one axial ligand and is the high-spin heme of HmcA (Fig. 3). This is because the short α -helix in the last cyt.*c*₃-like region of HmcA contains only one histidine, whereas the other histidine that would bind heme 15 is replaced by isoleucine 452 (HRKI in HmcA versus HRRH in 9HcA). The closest distance between Ile-452 and the iron atom of heme 15 is 3.4 Å to atom C⁶¹, which is a typical van der Waals contact distance. As a result, any enzymatic activity involving this heme group would require a conformational change to expose the free iron coordination site to the putative

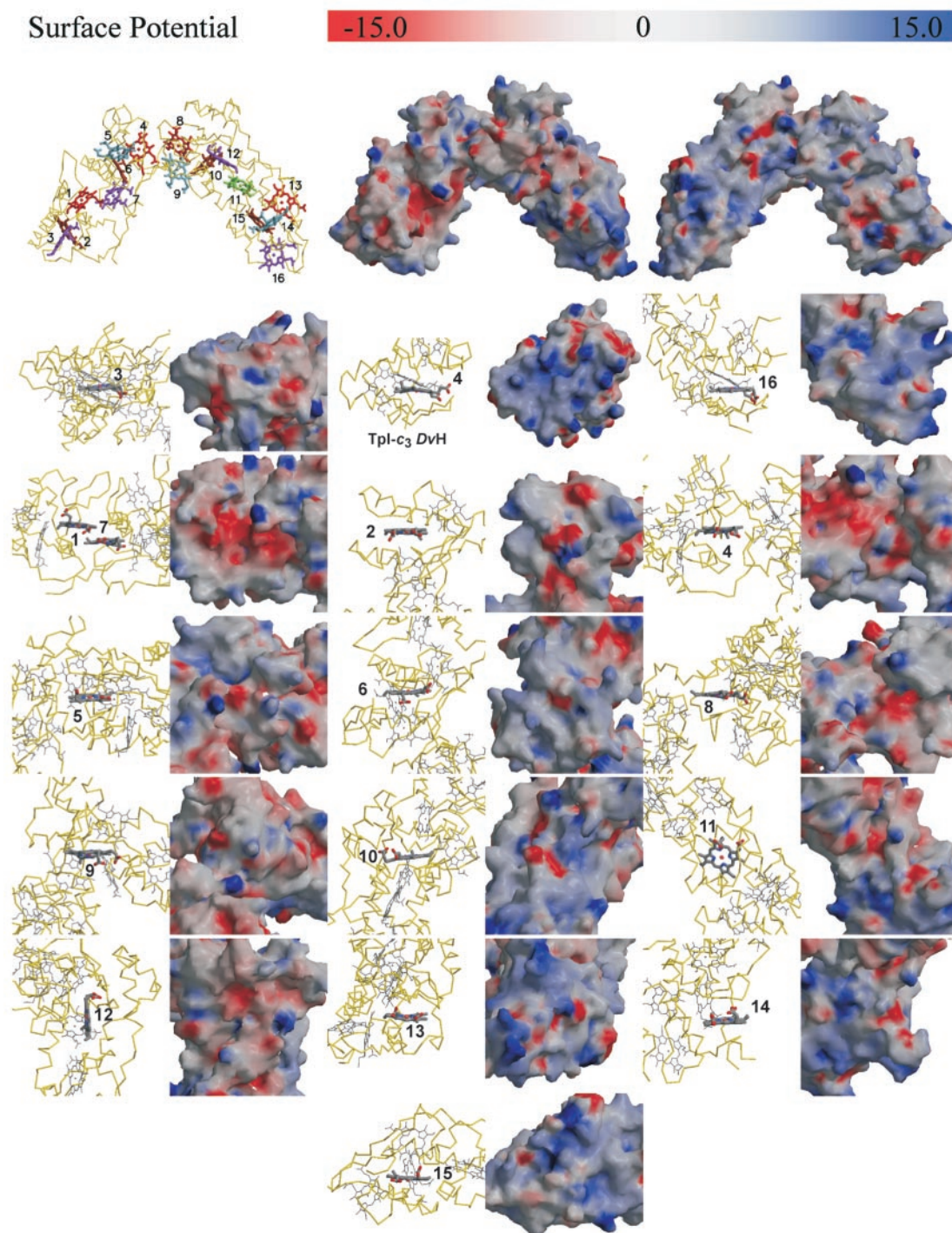


FIG. 4. **Electrostatic potential surface mapping at the molecular surface of the HmcA molecule.** Red zones correspond to negative potentials, whereas blue zones represent positive potentials. The range of potential spans from -15 to $+15$ kT/e . Two overall views are shown at the top, 180° apart about a vertical axis in the plane of the figure. Detailed views are included in the vicinity of each heme group. An equivalent picture for heme 4 of DvH Tpl-c₃ is also included for better comparison with hemes 3 and 16 of HmcA. Heme numbering is given by color code as in Fig. 1 for the first overall view and explicitly for the close-up views. The graphics were prepared with Molscript, Raster3D, GRASP (61–63).

substrate. So far, no evidence of such conformational change or enzymatic activity has been reported.

Surface Charge Distribution and Electron Transfer Sites—The electrostatic potential surface of the HmcA molecule (Fig. 4) shows that this molecule is less negatively charged overall than 9HcA (15) and the *Da* TpII-c₃ (18, 49). In addition, and in agreement with the poor reactivity of HmcA toward hydrogenase (26), the regions near the exposed parts of hemes 3 and 16 in HmcA (which correspond to cyt.c₃ heme 4 and are at each extremity of the molecule) lack the characteristic positive sur-

face patch around heme 4 of Tpl-c₃. There are several lysine residues in Tpl-c₃ (e.g. lysines 15, 57, 58, 60, 72, 94, 95, 101, and 102 in DvH Tpl-c₃ and lysines 16, 58, 59, 71, 94, 95, and 102 in Dd27k Tpl-c₃), which give rise to the positive surface area around heme 4 (see Fig. 4), responsible for its electron-transfer interaction with hydrogenase (18, 55). In contrast, around heme 3 of HmcA there are two lysine, two aspartic acid, and one glutamic acid residues (Lys⁵⁶, Asp⁵⁸, Lys¹⁰⁷, Glu¹⁰⁸, and Asp¹³²), which give the electrostatic potential surface a mix of positive and negative regions. Near HmcA heme 16

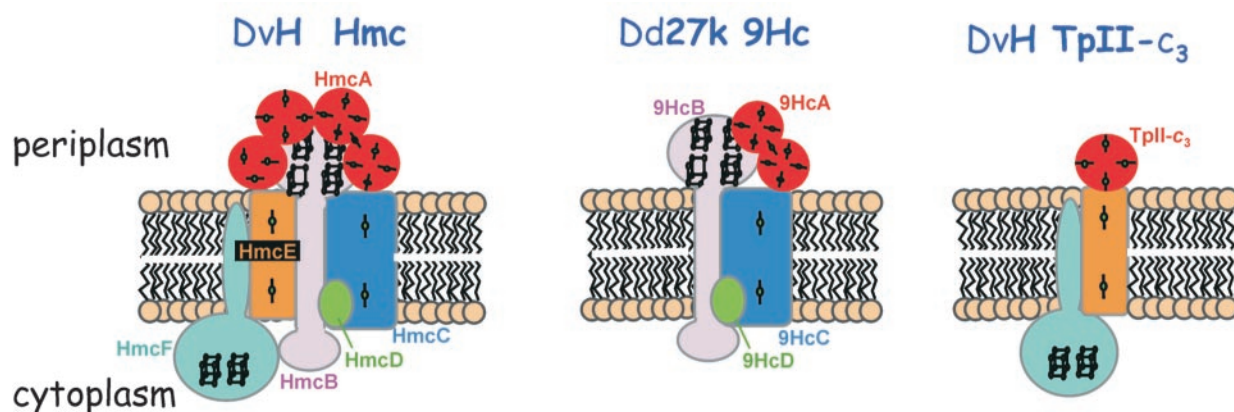


FIG. 5. Schematic models of the membrane-bound *DvH Hmc*, *Dd27k 9Hc*, and *DvH TpII-c₃* complexes drawn with the topology and redox centers for each protein as predicted from the gene sequence (see references in the text). Homologous proteins are represented with identical colors.

there are three lysine, one arginine, two glutamic acid, and one aspartic acid residues (Lys⁴⁴⁰, Glu⁴⁴¹, Lys⁵¹², Asp⁵²⁴, Glu⁵⁴², Arg⁵⁴³, and Lys⁵⁴⁵). Although the electrostatic potential surface in this zone is more predominantly positive than near heme 3, the contribution of the negatively charged residues is also important. Lys⁵⁴⁵ was not observed in the electron density maps and, therefore, was not included in the model. However, even though its contribution is missing from the calculated electrostatic potential surface of HmcA in the vicinity of heme 16, significant changes to these results are unlikely. The largest sections of negative electrostatic surface potential are located between the triheme and the tetraheme domains, in a region comprising hemes 1 and 7 (corresponding to hemes 1 and 4 of *cyt.c₃*), and around heme 8 (corresponding to heme 1 of *cyt.c₃*) at the top of the 9HcA domain. These negative surface regions are potential sites of interaction and electron exchange with the HmcA electron partners. The largest positive surface regions are located in the vicinity of hemes 13, 14, and 15 in the nine-heme domain of HmcA (which are hemes 1, 2, and 3 in *cyt.c₃* and 6, 7, and 8 in 9HcA) but have no correspondence in *TpIc₃*, *TpII-c₃* or 9HcA. The three cytochromes HmcA, 9HcA, and *TpII-c₃* share a common electron donor, the *TpI-c₃*, which acts as a mediator for electron transfer from hydrogenases. Indeed, catalytic amounts of this cytochrome increase the rate of reduction of either HmcA, 9HcA, or *TpII-c₃* by hydrogenases (16, 18, 26). This is particularly true in the case of *DvH HmcA* for which reduction by either of the three hydrogenases is extremely slow in the absence of *TpI-c₃* (26). Surface charge mapping of *TpII-c₃* (18) and 9HcA (15) indicates that they share similar characteristics that distinguish them from the *TpI-c₃*: contrary to *TpI-c₃*, heme 1 is exposed and surrounded by a negative surface region, whereas heme 4 (9HcA heme 9) lacks the *TpI-c₃* characteristic positive surface patch proposed to be the site of interaction with hydrogenases. The surface charge distribution of HmcA has similar characteristics to those of *TpII-c₃* and 9HcA.

For the case of the *Dd27K 9HcA*, modeling studies indicated a specific interaction between the negative heme 1 N-terminal region and the positive heme 4 region of *TpI-c₃* (15), a situation that may also occur for the *TpII-c₃*. Based on the hypothesis that the physiological electron donor to HmcA, 9HcA, and *TpII-c₃* is the *TpI-c₃* (16, 18, 26), on the modeling studies with 9HcA, and on the analysis of the other predicted proteins of the Hmc complex (see below), the present structure suggests that HmcA interacts with *TpI-c₃* at the surface region around heme 8 (equivalent to 9HcA heme 1), whereas the concave faces of the molecule and the N-terminal and C-terminal extremities are involved in interaction with the membrane-bound proteins of

the complex. The interaction between HmcA and *TpI-c₃* would require some conformational modification of HmcA with respect to the present structure, but this seems quite plausible given that heme 8 lies near the hinge between the two parts of the HmcA molecule, which are likely to have a high degree of flexibility between them. This high degree of flexibility may even be necessary to allow the HmcA molecule to attach to the transmembrane electron transfer complex, and it may be reasonably conceived that the overall shape of the molecule when attached to this complex is different from that observed in the crystal structure or as a free molecule in solution. The potential sites of interaction with the membrane-bound protein(s) of the complex are the HmcA terminal regions around heme 3 (with both negative and positive surface patches) and heme 16 (with both negative and positive surface patches), as well as the concave regions between hemes 1 and 7 (negative surface) and around the isolated heme 11 (two deep grooves with both negative and positive surface patches).

Physiological Role—The 16-heme HmcA, the 9-heme 9HcA, and the 4-heme *TpII-c₃* all have in common the fact that they are associated with membrane-bound redox complexes containing homologous proteins (Fig. 5). Sequencing of the 9HcA gene revealed the presence of a signal peptide (56), as observed for HmcA and *TpII-c₃*, indicating export to the periplasm. This gene is the first of a four gene operon (*9hc*) containing also *9hcB*, which is homologous to *hmcB* and has binding sites for four Fe₄S₄ clusters, *9hcC*, which is homologous to *hmcC* and codes for an integral membrane protein that may bind hemes *b* and interact with quinones, and *9hcD*, which codes for a small protein with similarities to HmcD (57). The gene coding for the *DvH TpII-c₃* was also identified in the preliminary data from the *DvH* genome (available at www.tigr.org), showing that it is adjacent to two genes coding for proteins homologous to the FeS protein HmcF and the membrane-bound HmcE, which may also bind hemes *b* (18). Also, the deposited sequence for the *Da TpII-c₃* gene includes part of an HmcF homologue.² Thus, all the similarities between the three cytochromes, HmcA, 9HcA, and *TpII-c₃*, and their associated complexes, suggest they may have a similar physiological function, which, according to the topology of the redox centers, is proposed to be electron transfer across the membrane and/or from the quinone pool for the cytoplasmic reduction of sulfate. The Hmc and the *TpII-c₃* complexes are both present in *DvH*, whereas the 9Hc complex is present in *Dd27K* and *DdE* where no HmcA or *TpII-c₃* was ever isolated. Given the similarity between 9HcA

² V. Magro, L. Pieulle, N. Forget, B. Guigliarelli, Y. Petillot, and E. C. Hatchikian (1997) EMBL:DACYTC3A, AC Y09718, GI:1770203.

and the two C-terminal nine-heme domains of HmcA, it was proposed that the 9Hc complex replaces the Hmc in *Dd27K* (16). Physiological studies have implicated HmcA specifically in the case where hydrogen is used as the sole energy source. Indeed, expression of the *hmc* operon increases when hydrogen is used as electron donor when compared with either lactate or pyruvate (23, 25). In *DvH* the *hmc* operon is adjacent to two genes (*rrf1* and *rrf2*) encoding expression-regulating proteins (21). A mutant containing a deletion of the *rrf1* and *rrf2* genes overexpresses the *hmc* operon three times, and it grows faster than the wild type on hydrogen but slower on lactate (23). A second mutant, in which the *hmc* operon is deleted, grows normally with lactate or pyruvate as electron donor (24), and it can still grow with hydrogen as the sole energy source but with a slower rate than the wild type. These results implicate the Hmc complex in the metabolism of hydrogen but not of lactate, and support the proposal that it is involved in the transfer of electrons from periplasmic hydrogen oxidation to the cytoplasmic reduction of sulfate. The fact that deletion of the *hmc* operon in *DvH* does not prevent growth on hydrogen indicates that there are other proteins that can fulfill the same role, and a likely candidate is the complex associated with the TpII-c₃ (18). Expression of the *9hc* operon in the facultative sulfate/nitrate reducer *Dd27K* is higher on sulfate than on nitrate, in agreement with a possible role of this complex as a substitute for the Hmc complex (57).

For the case of the HmcA the obvious question to pose is why is it necessary to have such a high number of hemes in one protein, especially if a proposed similar function is assumed for the smaller 9HcA. The HmcA biosynthesis must require a high energy investment for the cell, which would suggest that it has an important physiological role. Comparison of the genes present in the *hmc* operon with those of the *9hc* operon and the operon of the TpII-c₃ suggests that the Hmc complex has some sort of "bifunctionality" given that the type of redox centers seems to be duplicated relative to each of the other operons (Fig. 5). Indeed, a striking observation is that the Hmc complex contains two integral membrane proteins (HmcC and HmcE) related to the family of heme *b*-containing proteins, usually found associated with membrane-bound enzymatic complexes, and responsible for interaction with quinones (58). HmcE and HmcC are also related to each other, but HmcC is larger than HmcE. Homologues of each of these proteins are associated with each of the other two operons: the *9hc* operon has 9HcC, which is homologous to HmcC, whereas the operon of TpII-c₃ contains a homologue to HmcE. A similar situation is found for the FeS proteins with two such proteins being found in the *hmc* operon (HmcB and HmcF), whereas the *9hc* operon contains only 9HcB, homologous to HmcB, with the FeS clusters in the periplasm, and the operon of TpII-c₃ has a homologue to HmcF, with FeS clusters in the cytoplasm. Based on these observations it may be speculated that each of the two HmcA regions will interact with different membrane-bound proteins: the 9HcA domain of HmcA may interact with HmcB and HmcC, whereas the first two domains of HmcA may be involved in interaction with HmcE and HmcF. The multitude of redox centers indicated by genes of the *hmc* operon also suggests that there may be several electron transfer points in this complex, namely in the periplasm (via HmcA and/or HmcB), in the membranes (via HmcC and/or HmcE) and in the cytoplasm (via HmcF). This situation is also observed in the operon of the TpII-c₃, but may be more limited for the *9hc* operon, which is missing a redox protein in the cytoplasm. An interesting model has been proposed for the function of the Hmc proteins, in which HmcA, HmcB, and HmcC are proposed to act as a menaquinol reductase using electrons derived from periplasmic ox-

idation of hydrogen, whereas HmcE and HmcF are proposed to act as a menaquinol oxidase transferring electrons for the cytoplasmic reduction of sulfate (59). This would agree with the proteins found in the 9HcA complex, but not with the TpII-c₃ complex in which homologues of HmcE and HmcF are associated with the periplasmic TpII-c₃, suggesting electron transfer with periplasmic proteins.

In conclusion, the present structure of *DvH* HmcA fully supports predictions for its arrangement in four cyt.c₃-like regions, two of which form a larger 9HcA domain. A detailed analysis of this structure reveals several points of similarity between HmcA and the 9HcA and TpII-c₃ molecules, which agree with their similar genetic organization and mode of reactivity, and further support a similar physiological function for the three cytochromes that involves electron transfer across the membrane from the periplasm or the quinone pool to the cytoplasm. The fact that *DvH* and *Dg* HmcA both contain high-spin hemes suggested that this protein could also have an enzymatic function. However, such a function could never be found (14, 60), and the present structure also argues against this possibility, because the space above the iron atom in the high-spin heme 15 is not accessible to a substrate. Furthermore, a high-spin heme is not observed in the 9HcA, so it is possible that HmcA heme 15 could have lost its His ligand without the loss affecting its physiological function. The multitude of redox centers in both HmcA and other proteins of the Hmc complex also suggests the possibility of multiple electron donors to this complex.

Acknowledgments—We thank João Carita and the staff of the Instituto de Biologia Experimental e Tecnológica. Fermentation Plant for growing the bacterial cells and Susana Sousa (Instituto de Tecnologia Química e Biológica, Universidade Nova de Lisboa (ITQB-UNL)) for helping in the preparation of the crystals used for data collection. Thanks are also due to ESRF and to Dr. Andrew Thompson (EMBL, Grenoble) for financial and technical support, respectively, during the data collection at the Joint Structural Biology Group ID-29 beamline. Helpful discussions and suggestions with Dr. Claudio M. Soares (ITQB-UNL) are also gratefully acknowledged.

REFERENCES

- Hamilton, W. A. (1998) *Biodegradation* **9**, 201–212
- Loubinoux, J., Bronowicki, J. P., Pereira, I. A. C., Mougénel, J. L., and Le Faou, A. E. (2002) *FEMS Microbiol. Ecol.* **1341**, 1–6
- Brandis, A., and Thauer, R. K. (1981) *J. Gen. Microbiol.* **126**, 249–252
- Postgate, J. R. (1984) *The Sulphate Reducing Bacteria*, 2nd Ed., pp. 56–100, Cambridge University Press, United Kingdom
- Tsuji, K., and Yagi, T. (1980) *Arch. Microbiol.* **125**, 35–42
- Traore, A. S., Hatchikian, C. E., Bélaich, J. P., and LeGall, J. (1981) *J. Bacteriol.* **154**, 101–109
- Odom, J. M., and Peck, H. D., Jr. (1981) *FEMS Microbiol. Lett.* **12**, 47–50
- Louro, R. O., Catarino, T., Turner, D. L., Piçarra-Pereira, M. A., Pacheco, I., LeGall, J., and Xavier, A. V. (1998) *Biochemistry* **37**, 15808–15815
- Louro, R. O., Bento, I., Matias, P. M., Catarino, T., Baptista, A. M., Soares, C. M., Carrondo, M. A., Turner, D. L., and Xavier, A. V. (2001) *J. Biol. Chem.* **276**, 44044–44051
- Higuchi, Y., Inaka, K., Yasuoka, N., and Yagi, T. (1987) *Biochim. Biophys. Acta* **911**, 341–348
- Brent, W., and Voordouw, G. (1991) *J. Bacteriol.* **173**, 220–228
- Ogata, M., Kiuchi, N., and Yagi, T. (1993) *Biochimie* **75**, 977–983
- Chen, L., Pereira, M. M., Teixeira, M., Xavier, A. V., and LeGall, J. (1994) *FEBS Lett.* **347**, 295–299
- Pereira, I. A. C., LeGall, J., Xavier, A. V., and Teixeira, M. (1997) *J. Biol. Inorg. Chem.* **2**, 23–31
- Matias, P. M., Saraiva, L. M., Soares, C. M., Coelho, A. V., LeGall, J., and Carrondo, M. A. (1999) *J. Biol. Inorg. Chem.* **4**, 478–494
- Matias, P. M., Coelho, R., Pereira, I. A. C., Coelho, A. V., Thompson, A. W., Sieker, L. C., LeGall, J., and Carrondo, M. A. (1999) *Structure* **7**, 119–130
- Umhu, S., Fritz, G., Diederichs, K., Breed, J., Welte, W., and Kroneck, P. M. (2001) *Biochemistry* **40**, 1308–1316
- Valente, F. M. A., Saraiva, L. M., LeGall, J., Xavier, A. V., Teixeira, M., and Pereira, I. A. C. (2001) *ChemBioChem* **2**, 895–905
- Frazão, C., Sieker, L. C., Sheldrick, G., Lamzin, V., LeGall, J., and Carrondo, M. A. (1999) *J. Biol. Inorg. Chem.* **4**, 162–165
- Matias, P. M., Morais, J., Coelho, A. V., Meijers, R., Gonzalez, A., Thompson, A. W., Sieker, L., LeGall, J., and Carrondo, M. A. (1997) *J. Biol. Inorg. Chem.* **2**, 507–514
- Rossi, M., Pollock, W. B. R., Reij, M. W., Keon, R. G., Fu, R., and Voordouw, G. (1993) *J. Bacteriol.* **175**, 4699–4711
- Keon, R. G., and Voordouw, G. (1996) *Aerobe* **2**, 231
- Keon, R. G., Fu, R., and Voordouw, G. (1997) *Arch. Microbiol.* **167**, 376–383
- Dolla, A., Pohorelic, B. K. J., Voordouw, J. K., and Voordouw, G. (2000) *Arch.*

- Microbiol.* **174**, 143–151
25. Steger, J. L., Vincent, C., Ballard, J. D., and Krumholz, L. R. (2002) *Appl. Environ. Microbiol.* **68**, 1932–1937
26. Pereira, I. A. C., Romão, C. V., Xavier, A. V., LeGall, J., and Teixeira, M. (1998) *J. Biol. Inorg. Chem.* **3**, 494–498
27. Matthews, B. W. (1968) *J. Mol. Biol.* **33**, 491–497
28. Otwinowski, Z., and Minor, W. (1997) *Methods Enzymol.* **276**, 307–326
29. Collaborative Computational Project Number 4 (1994) *Acta Crystallogr. Sect. D Biol. Crystallogr.* **50**, 760–763
30. Weeks, C. M., and Miller, R. (1999) *J. Appl. Crystallogr.* **32**, 120–124
31. Otwinowski, Z. (1991) in *Proceedings of the CCP4 Study Weekend* (Wolf, W., Evans, P. R., and Leslie, A. G. W., eds) pp. 80–86, SERC Daresbury Laboratory, Warrington, UK
32. Cowtan, K. (1994) *Joint CCP4 and ESF-EACMB Newsl. Protein Crystallogr.* **31**, 34–38
33. Terwilliger, T. C., and Berendzen, J. (1999) *Acta Crystallogr. Sect. D Biol. Crystallogr.* **55**, 849–861
34. Terwilliger, T. C. (2001) *Acta Crystallogr. Sect. D Biol. Crystallogr.* **57**, 1755–1762
35. Jones, T. A., Zou, J. Y., Cowan, S. W., and Kjeldgaard, M. (1991) *Acta Crystallogr. Sect. A* **47**, 110–119
36. Roussel, A., Fontecilla-Camps, J. C., and Cambillau, C. (1990) in *XV International Union of Crystallography Congress Abstracts*, pp. 66–67, Bordeaux, France
37. Brünger, A. T. (1992) *X-PLOR, Version 3.1: a System for Crystallography and NMR*, Yale University Press, New Haven
38. Brünger, A. T. (1992) *Nature* **355**, 472–474
39. Lamzin, V. S., and Wilson, K. S. (1997) *Methods Enzymol.* **277**, 269–305
40. Perrakis, A., Sixma, T. K., Wilson, K. S., and Lamzin, V. S. (1997) *Acta Crystallogr. Sect. D Biol. Crystallogr.* **53**, 448–455
41. Read, R. J. (1986) *Acta Crystallogr. Sect. A* **42**, 140–149
42. Murshudov, G. N., Vagin, A. A., and Dodson, E. J. (1997) *Acta Crystallogr. Sect. D Biol. Crystallogr.* **53**, 240–255
43. Schomaker, V., and Trueblood, K. N. (1968) *Acta Crystallogr. Sect. B Struct. Sci.* **24**, 63–76
44. Berman, H. M., Westbrook, J., Feng, Z., Gilliland, G., Bhat, T. N., Weissig, H., Shindyalov, I. N., and Bourne, P. E. (2000) *Nucleic Acids Res.* **28**, 235–242
45. Tickle, I. J., Laskowski, R. A., and Moss, D. S. (1998) *Acta Crystallogr. Sect. D Biol. Crystallogr.* **54**, 547–557
46. Laskowski, R. A., MacArthur, M. W., Moss, D. S., and Thornton, J. M. (1993) *J. Appl. Crystallogr.* **26**, 283–291
47. Ramachandran, G. N., and Sasisekharan, V. (1968) *Adv. Prot. Chem.* **23**, 283–437
48. Morris, A. L., MacArthur, M. W., Hutchinson, E. G., and Thornton, J. M. (1992) *Proteins* **12**, 345–364
49. Nørager, S., Legrand, P., Pieulle, L., Hatchikian, C., and Roth, M. (1999) *J. Mol. Biol.* **290**, 881–902
50. Pieulle, L., Haladjian, J., Bonicel, J., and Hatchikian, E. C. (1996) *Biochim. Biophys. Acta* **1273**, 51–61
51. Magro, V., Pieulle, L., Forget, N., Guigliarelli, B., Petillot, Y., and Hatchikian, E. C. (1997) *Biochim. Biophys. Acta* **1342**, 149–163
52. Simões, P., Matias, P. M., Morais, J., Wilson, K., Dauter, Z., and Carrondo, M. A. (1998) *Inorg. Chim. Acta* **273**, 213–224
53. Czjzek, M., Arnoux, P., Haser, R., and Shepard, W. (2001) *Acta Crystallogr. Sect. D Biol. Crystallogr.* **57**, 670–678
54. Coutinho, I. B., Turner, D. L., Liu, M.-Y., LeGall, J., and Xavier, A. V. (1996) *J. Biol. Inorg. Chem.* **1**, 305–311
55. Matias, P. M., Soares, C. M., Saraiva, L. M., Coelho, R., Morais, J., LeGall, J., and Carrondo, M. A. (2001) *J. Biol. Inorg. Chem.* **6**, 63–81
56. Saraiva, L. M., da Costa, P. N., and LeGall, J. (1999) *Biochem. Biophys. Res. Commun.* **262**, 629–634
57. Saraiva, L. M., da Costa, P. N., Conte, C., Xavier, A. V., and LeGall, J. (2001) *Biochim. Biophys. Acta* **93546**, 1–8
58. Berks, B. C., Page, M. D., Richardson, D. J., Reilly, A., Cavill, A., Outen, F., and Ferguson, S. J. (1995) *Mol. Microbiol.* **15**, 319–331
59. Richardson, D. J. (2000) *Microbiology* **146**, 551–571
60. Verhagen, M. F. J. M., Pierik, A. J., Wolbert, R. B. G., Mallée, L. F., Voorhorst, W. G. B., and Hagen, W. R. (1994) *Eur. J. Biochem.* **225**, 311–319
61. Kraulis, P. J. (1991) *J. Appl. Crystallogr.* **24**, 946–950
62. Merritt, E. A., and Murphy, M. E. P. (1994) *Acta Crystallogr. Sect. D Biol. Crystallogr.* **50**, 869–873
63. Nicholls, A. (1992) *GRASP: Graphical Representation and Analysis of Surface Properties*, Columbia University, New York